

Comparing Orientation Analysis Methods for a Shallow-Water Ocean-Bottom Seismometer Array in the Bohai Sea, China

Weiwei Xu^{*1}, Songyong Yuan¹, Weitao Wang¹, Xinheng Luo², and Li Li¹

ABSTRACT

The horizontal orientation estimation of an ocean-bottom seismometer (OBS) is critical for providing reliable data for seismological studies. In this article, we applied three independent polarization analysis methods to estimate the absolute horizontal orientation of a pilot shallow-water OBS array in Bohai Sea, China. The OBS array was deployed in the autumn of 2018 and comprised 32 broadband seismometers lasting around 1 yr, aimed at investigating the geodynamics of North China craton and adjacent areas. The timings of the data were corrected through the correlation analysis of regional and teleseismic earthquake events, before the polarization analysis. Polarization analysis using *P* wave and Rayleigh wave, from both natural earthquakes and noise cross correlations, was performed. In total, 28 out of 29 stations obtained the effective estimates combining the three methods, of which 11 stations showed relatively robust results with variations well below 10° among the three methods. However, the superiority of one method over the others is not obvious. As there is a trade-off between the accepted final estimates and the number of qualified measurements defined by parameters such as the correlation coefficient threshold, window length, and filtering options, we investigated these effects using 15 different groups of parameters for the three methods, and the deviation statistics showed a distribution with the root mean square deviation of 9.2° for the whole array.

KEY POINTS

- An OBS array in the Bohai Sea is used to compare orientation analysis methods for horizontal components.
- We test three independent methods, and sometimes find disagreement of up to 40 degrees between methods.
- The combination of three methods proves robust for determining most orientations within 25 degrees.

Supplemental Material

INTRODUCTION

The Bohai Sea, located in the eastern North China craton (NCC), is one of the most productive petroleum areas in China; moreover, it serves as an important window to understand NCC-related geodynamics, such as the NCC destruction time, scale, and its mechanisms, which recently aroused great interest in the geoscientific community (Zhu *et al.*, 2012; Wu *et al.*, 2019). Most previous studies were based on geological and geophysical surveys at adjacent land areas of the Bohai Sea, thus implying that the greatest extension might occur in the center of the Bohai Sea (Hou and Hari, 2014), together with the thinnest lithosphere (Chen *et al.*, 2008). Two

onshore–offshore wide-angle seismic profiles were obtained, using a high-frequency ocean-bottom seismometer (OBS) with an air-gun source to image the crust structure in 2010 and 2011, with each experiment lasting for about two weeks (Liu *et al.*, 2015). The year-long broadband OBS array experiment, generally considered one of the most powerful tools to understand the mantle structure and dynamic process, had not been implemented before 2018, thus obscuring interpretations of the exact geodynamics deep underground.

The biggest challenges facing the long-term passive seismic OBS array in the Bohai Sea stem from three aspects: frequent bottom-trawling events attributed to the fishery industry, strong ocean current due to the shallow-water body, and severe corrosions caused by all types of local seashells. In 2018, a novel three-component broadband OBS was specially developed for Bohai Sea-like environments by Zhuhai Taide Enterprise Co. Ltd. An ~500 kg slope-shaped coupling frame

1. Institute of Geophysics, China Earth Administration, Beijing, China; 2. Zhuhai Taide Enterprise Co. Ltd., Zhuhai, China

*Corresponding author: wxuwww@sina.com

Cite this article as Xu, W., S. Yuan, W. Wang, X. Luo, and L. Li (2020). Comparing Orientation Analysis Methods for a Shallow-Water Ocean-Bottom Seismometer Array in the Bohai Sea, China, *Bull. Seismol. Soc. Am.* **XX**, 1–11, doi: [10.1785/0120200174](https://doi.org/10.1785/0120200174)

© Seismological Society of America

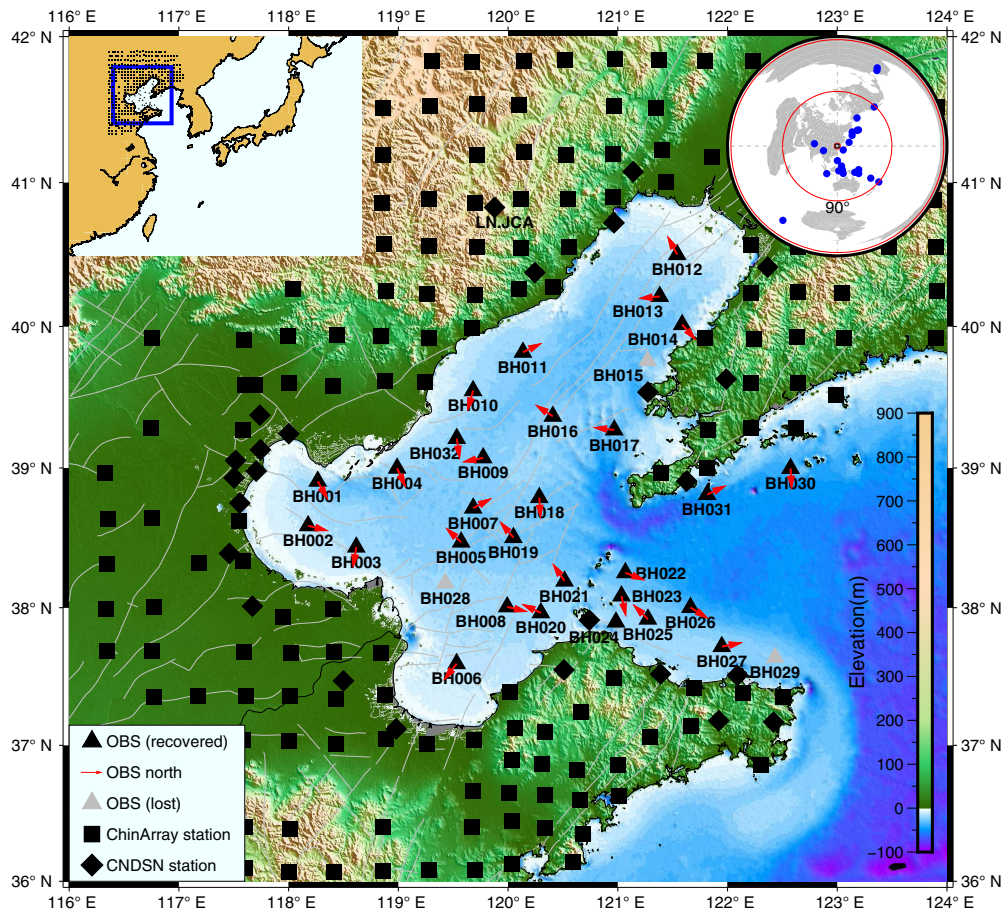


Figure 1. Station and earthquake locations used in this study. The 29 recovered ocean-bottom seismometer (OBS) stations are denoted as black triangles, together with an arrow attached showing the determined real north direction of the seismometer in this study; the three lost OBS are shown as gray triangles. The nearby 27 Chinese National Digital Seismographic Network (CNDSN) stations are denoted as black diamonds, which are used mainly for time correction, and the 325 ChinArray stations are denoted as black squares, which are used in orientation determination with ambient-noise technique. Earthquakes used are shown as dots in the upper-right inset used for the P -wave and Rayleigh-wave analyses. The upper-left inset shows a larger map of the study area with all the seismic stations used in this paper shown as black dots. Gray lines show the fault distribution in the area (Deng *et al.*, 2003), and the background colors represent the topography, together with the lower-right color bar showing the altitude scale. The color version of this figure is available only in the electronic edition.

made of a composite of concrete and anti-erosion steel was designed to provide gravitational stability and mitigate the surge from strong ocean currents, and, the seismometer package was located in the center and connected with the outside frame using soft Kevlar leashes, providing both high intensity and chemical stability; furthermore, a mechanic gadget was always embedded to maintain sufficient gap between the middle seismometer and surrounding frame. In the autumn of 2018, in all, 32 sets of such OBSs were deployed in the Bohai Sea, as shown in Figure 1 and gradually recovered from June to September in 2019. Finally, 29 of the 32 stations (~90%) were successfully recovered.

The orientation of the horizontal components needs to be determined for seismic records in many seismic applications, such as receiver functions, surface-wave dispersion, and

analysis of anisotropy, which use a three-component seismometer. For free-fall OBS deployment, the vertical component can be appropriately aligned with the gravitational field, using controllable electronics in virtue of motor-driven gimbal and tilt sensors. However, the azimuthal orientations of two horizontals remain unknown, owing to the lack of control during installation. Determination of the orientation of horizontal components is usually the first step before applying the OBS data within the research areas, as mentioned earlier.

Various orientation-estimation methods have been proposed previously. In the late 1980s, air-gun shots were successfully used to retrieve the horizontal orientation of OBS from known locations (Anderson *et al.*, 1987); however, these are not available in most passive experiments. By analyzing the polarization of long-period teleseismic surface waves, Laske quantified the azimuthal misorientations of terrestrial stations using a nonlinear inversion (Laske, 1995). Many researchers exploited the particle-motion characteristics of P waves to orient the seismometer, including examining the first-arrival particle motion (Schulte-Pelkum *et al.*, 2001) and minimizing

the transverse energy of seismic record in a selected window (Niu and Li, 2011; Wang *et al.*, 2016); the latter is also widely used in single-station P -wave earthquake early warning areas (Fontaine *et al.*, 2009). Ekström and Busby determined the arrival angle by calculating the correlation between the surface-wave time series and the synthetic waveform generated using previously calculated moment tensor solutions (Ekström and Busby, 2008). An automated procedure was developed to measure the arrival angles of the first-arriving Rayleigh wave; it is currently used by the Ocean Bottom Seismograph Instrument Center facility to provide OBS orientation estimates (Stachnik *et al.*, 2012). Based on ambient noise consisting of mainly Rayleigh waves, Zha *et al.* presented a method to orient OBS by cross-correlating the Green's function cross and diagonal terms between station pairs (Zha *et al.*, 2013). A recent study

effectively determined OBS orientation with polarity flipping errors combining polarization analysis and waveform modeling (Zhu *et al.*, 2020).

Previous experiments and studies have shown that a shallow-water OBS usually exhibits relatively higher noise levels at periods >10 s, compared with deep-water OBS, owing to strong currents and the nearby ocean surface (Webb and Crawford, 2010; Sumy *et al.*, 2015), which deteriorates the earthquake identification signal from ambient noise in many seismic applications, including multiple orientation determination techniques mentioned previously. In this article, we apply three independent orientation methods to retrieve the horizontal orientation of OBS in the Bohai Sea. We expect these three techniques to complement each other and help acquire effective results; furthermore, the result consistencies among the three techniques could be studied, and help better understand the validity and error evaluation of the seismometer orientations obtained. The three methods are all based on polarization analysis, and they are chosen because of their simple implementations and no requirement of synthetic waveforms or precise earthquake source parameters. The methods include particle-motion analysis of *P* and Rayleigh waves from earthquake events and Rayleigh waves extracted from cross correlation of ambient seismic noise. They will be elaborated in the following sections.

DATA PREPARATION

Figure 1 shows the station locations and earthquake events used in this study. Besides the 29 OBS stations in the Bohai Sea, 27 permanent broadband seismic stations from the Chinese National Digital Seismographic Network (CNDSN) are shown as black diamonds, which are used for the time correction discussed hereafter. During the operation period of the OBS array in the Bohai Sea, the ChinArray project, which has a concept similar to that of the USArray project and aims to cover the entire mainland of China by broadband seismic observation, comes at its third phase in the North China area. Three hundred and twenty-five stations from the ChinArray project are shown as black squares and are used in orientation determination for ambient-noise analysis to increase ray-path coverage, thus hopefully improving the validity of the result.

Unlike the land seismic station, in which the correct absolute timing can usually be ensured by frequent synchronization between the internal clock and Global Positioning System (GPS) signal, the timing in OBS can only be synchronized with the GPS twice, that is, immediately before deployment and after recovery, since the GPS satellite signal does not reach the seafloor. In our case, the first synchronization was well done, as expected, for all the stations. However, the second one made little or even no sense for most stations, after we examined the data after recovery. The tricky thing is that most stations stopped recording data two or three months before the

recovery, and the acquisition system was found to have been rebooted many times. Now, the reason has been technically attributed to the malfunction of hardware watch-dog design and flashcard writing algorithm with bad blocks. Although the deficit will and can be corrected in the subsequent development, we must face the issue of how to fix the data timing so as not to influence the determination of seismometer orientation.

We chose to employ a correlation analysis of earthquake events between stations to correct the OBS timing. Twenty-seven nearby CNDSN stations were selected as references, due to their high timing accuracies from the continuous GPS synchronization. During the operation period, we selected earthquakes of magnitude ≥ 5 , and epicentral distance within 5° and 90° were selected; and altogether 21 earthquake events with clear first-arrival *P* wave were left for later analysis after a careful visual check—of all the OBSs in the Bohai Sea and nearby CNDSN stations. An example was shown, as in Figure 2, the waveforms of vertical components from the 27 CNDSN land stations and 29 OBS stations were filtered between 0.1 and 2 Hz, using a zero-phase Butterworth filter, and aligned as the first-arrival *P* wave estimated, based on the isap91 model (Kennett, 1991), in the order of epicentral distance. The shown earthquake waveforms were recorded more than three months after the deployments and visually showed high signal-to-noise ratios (SNRs) and similarities between stations; an exception came from station BH017, with epicentral distance $\sim 33.04^\circ$, showing a timing difference of ~ 5 s from others.

For all selected vertical components of earthquake events, we chose station LN.JCA from the 27 CNDSN stations as reference station, due to both its high SNR and good timing quality. For each earthquake, a waveform window was selected from the right beginning of initial *P*-wave arrival to 30 s after for the reference station and all the other stations (the rest 26 CNDSN stations and 29 OBS stations), correlation analysis was performed between each pair of waveform window, and a timing offset could be obtained by maximizing the correlation coefficient through sliding windows. The differences of the theoretic *P*-wave arrivals between each station and the reference station LN.JCA can be seen as an indication of clock error for each station, if we neglect the local lateral heterogeneities, which turns out not to be the dominant factor in our results, as we will show later. During correlation analysis, two thresholds were set to filter the results. One is the SNR, which we defined as the energy ratio between two waveform windows before and after the initial *P*-wave arrival, set as 5. The other one is the maximum correlation coefficient, set as 0.6. After computations, we visually rechecked the corresponding waveforms to filter out those results caused by abnormal signals; during this process, only a few outliers were picked out, which proved that the two thresholds selected were quite reasonable.

Figure 3 shows the results we obtained from the correlation analysis, and the most prominent feature is that clock error

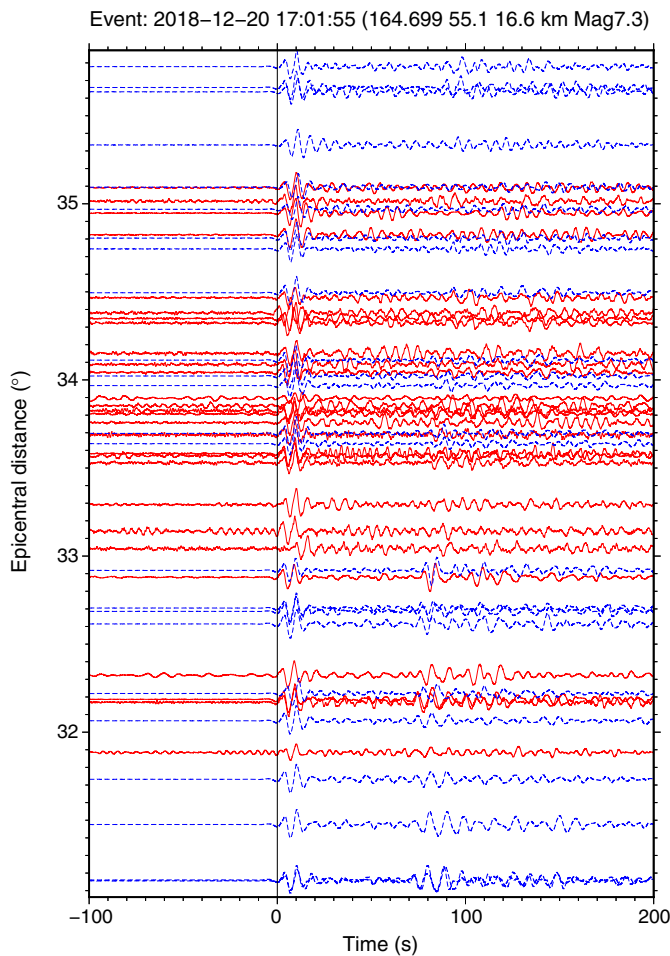


Figure 2. The initial P -wave signals for the 27 CNDSN stations (dashed lines) and the 29 OBS stations (solid lines) from an earthquake of M_w 7.3, origin time at 17:01:55, 20 December 2018. The waveforms are aligned as initial P -wave arrival at zero-second estimated based on the iasp91 model and plotted in the order of epicentral distances. The color version of this figure is available only in the electronic edition.

variation for most stations performed well before around April 2019, except for three OBS stations; however, a sudden rise of clock error occurred for many OBS stations after around April 2019, which is proved to be due to the malfunction of data acquisition system mentioned earlier. The structure heterogeneity or anisotropy underground in the study area may influence the clock errors obtained in Figure 3. Nonetheless, these contributions are limited to a confined range, such as 1–2 s at most, after we examined the results before April 2019, as shown in the magnified inset of Figure 3. Because all the CNDSN stations have high-accuracy timing services ensured by the continuous GPS synchronization, we can assert that the timing accuracies of all stations are well below 2 s before April 2019, except for three abnormal OBS stations. Such a level of timing accuracies is better than expected. We conclude that it stems from two reasons. One is the fact that the quartz oscillator inside the acquisition system depends mainly on ambient

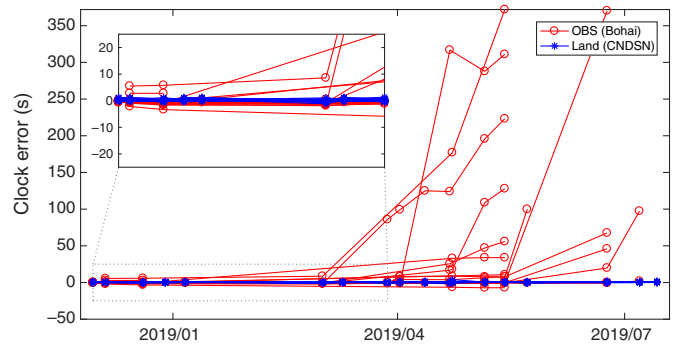


Figure 3. Clock error and its variations determined from the initial P -wave correlation analysis for the 29 OBS and 27 land stations. Circles denote the results for the OBS stations in the Bohai Sea, and asterisks denote the results for the CNDSN stations. The inset shows an enlarged view of the part framed by the dotted lines. The color version of this figure is available only in the electronic edition.

temperature, which is relatively stable in seafloor. The other is due to a novel built-in feature of temperature-compensation, self-learning design in timing service electronics developed in the OBS.

We applied the clock errors obtained here to time corrections of all earthquake events used for P - and Rayleigh-wave particle-motion analysis. The timing accuracies of such a level would not have a substantial influence on the final results of orientation determination, considering that we had a manual pick on the P -wave window for the P -wave analysis and adopted a relatively long time window, which had a good tolerance for a few seconds offset for Rayleigh-wave analysis (Stachnik *et al.*, 2012). For the ambient-noise analysis, we only used the data before April 2019, we did not include those data with hardware malfunction, in case they obscure the final determinations due to significant potential errors even after the timing correction.

P-WAVE POLARIZATION ANALYSIS

As shown in Figure 4, we use a coordinate system to show the relation between seismometer components and seismic signals. Throughout this article, the horizontal orientation of the OBS is defined as the clockwise angle from the geographic north to the station's H1 (or nominal north–south) component, with H2 (or nominal east–west) oriented 90° clockwise from H1, consistent with the right coordinate convention of the International Federation of Digital Seismograph Networks.

In a laterally isotropic, homogeneous medium, the particle motion of compressional P wave is confined in the vertical plane containing the source and receiver and absent in the transverse component. For a misoriented OBS station, the best angle Φ can be obtained by minimizing the energy in the transverse component through rotating the nominal northeast coordinate to radial–transverse coordinate. This process can be equalized as solving a problem of variance maximization in

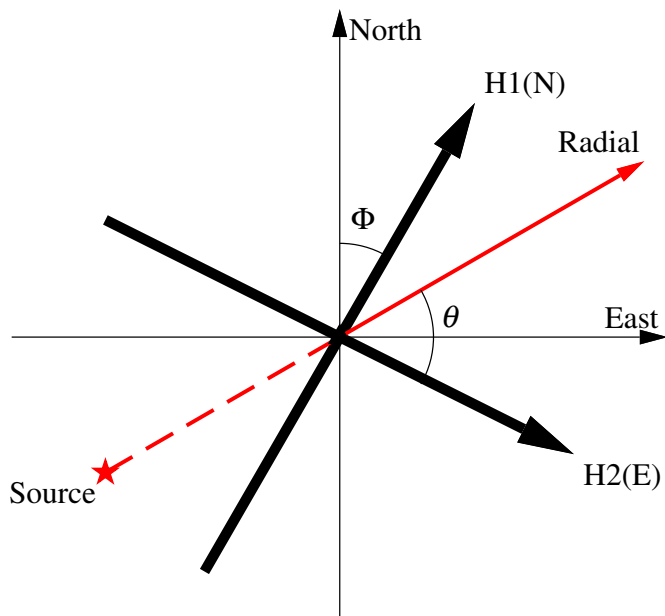


Figure 4. A schematic plot of the coordinate system showing the relation of seismometer components and seismic signals. H1(N) and H2(E) represent the unknown direction of orthogonal OBS components, and Φ represents the angle clockwise from the geographic north to H1 (or nominal north-south) component of OBS. Source labeled can be either a real earthquake event or a virtual source of Rayleigh wave propagated from. The convention is used for all the three polarization methods in this article. The color version of this figure is available only in the electronic edition.

a way called principal component analysis, which is well known in statistical analysis (Jurkevics, 1988; Niu and Li, 2011). For a suite of earthquake events recorded at an OBS station, we employ the SNR-weighted-multievent method to obtain the best angle Φ by minimizing the weighted summation of the transverse P -wave energy ($E_T(\Phi)$) from all the events (Niu and Li, 2011), given by

$$E_T(\Phi) = \frac{\sum_{i=1}^N \omega_i E_T^i(\Phi)}{\sum_{i=1}^N \omega_i}, \quad (1)$$

in which the weight ω_i is the average SNR of two horizontal components, and N is the total number of the events. The 180° ambiguity discrepancy is solved by cross-correlating the vertical and horizontal components and choosing the azimuth showing a positive correlation.

The earthquakes used included the teleseismic events of magnitude ≥ 6.0 , with epicentral distances between 30° and 90° , and the regional events of magnitude ≥ 5.0 , with epicentral distances between 5° and 30° (see Table S1 to find earthquake details used in the supplemental material of this article). The regional events with shorter distances ($\leq 5^\circ$) could contribute large errors to the results due to the epicentral mislocation uncertainty (Wang et al., 2016), and the teleseismic events with greater distances ($\geq 90^\circ$) do not have high SNR due to relatively weak P -wave signal, hence are not included.

We visually examined all the selected waveform data and only maintained those showing clear initial P -wave arrival. Meanwhile, we manually updated the P -wave arrivals to a higher accuracy, although they were estimated by iasp91 model before. Next, we deconvolved the instrument responses from the data to restore the ground displacement, removed the mean and trend, and then band-pass filtered from 0.04 to 0.1 Hz for later analysis. Figure 5 shows an example of the analysis procedure for station BH010. For the two horizontal components, the lengths of the waveform window for both signal and noise are set as 25 s. Best angle 195° was obtained by minimizing the summed energy of transverse components from all the events at the station. We estimated the uncertainty following Niu and Li (2011), which defines it as the 95% confidence level for 1 degree of freedom per second. Table 1 listed all the results, including the number of earthquakes used, the obtained orientation angles, and their errors for each station, respectively.

Apart from the above-mentioned weight-summing method, another strategy in P -wave polarization analysis is based on the single earthquake waveform, and the zero-lag cross-correlation coefficients (CCs) between the vertical and radial components are used as the quality control factors to select qualified results (Wang et al., 2016). We varied CCs from 0.5 to 0.9 with an interval of 0.1 and showed the results in Table S2 and Figure S1. When setting CC as 0.8, only 13 stations obtained the effective estimates, and just a few earthquakes met the criteria and contributed to the determination. In Table S2 and Figure S1, we also included the weight-summing results removing earthquakes between 5° and 30° , to evaluate the possible influences from the locally lateral heterogeneities at these distances; the results show that the differences are well below 5° for most stations except station BH011, and the few number of regional earthquakes (only five) inhibit us from studying these effects deeply. Hereafter, we use the P -wave weight-summing results with the earthquakes between 5° and 90° , to compare with the results obtained from other techniques.

RAYLEIGH-WAVE POLARIZATION ANALYSIS

Theoretically, fundamental Rayleigh wave propagates with a retrograde elliptical particle motion, and can only be observed on the vertical and radial components. Thus, by measuring the ellipticity of the incoming Rayleigh wave with known azimuth, the horizontal direction of the seismometer can be solved. This method is substituted by a simpler and stable way through the Rayleigh-wave polarization analysis, by maximizing the cross correlations between the vertical and the Hilbert-transformed radial component due to the nature of the 90° phase shift of Hilbert transformation. The correlation coefficient is defined as follows (Baker and Stevens, 2004; Stachnik et al., 2012):

$$C_{z\bar{r}}(\Phi) = \frac{S_{z\bar{r}}}{\sqrt{S_{zz}S_{\bar{r}\bar{r}}}}, \quad (2)$$

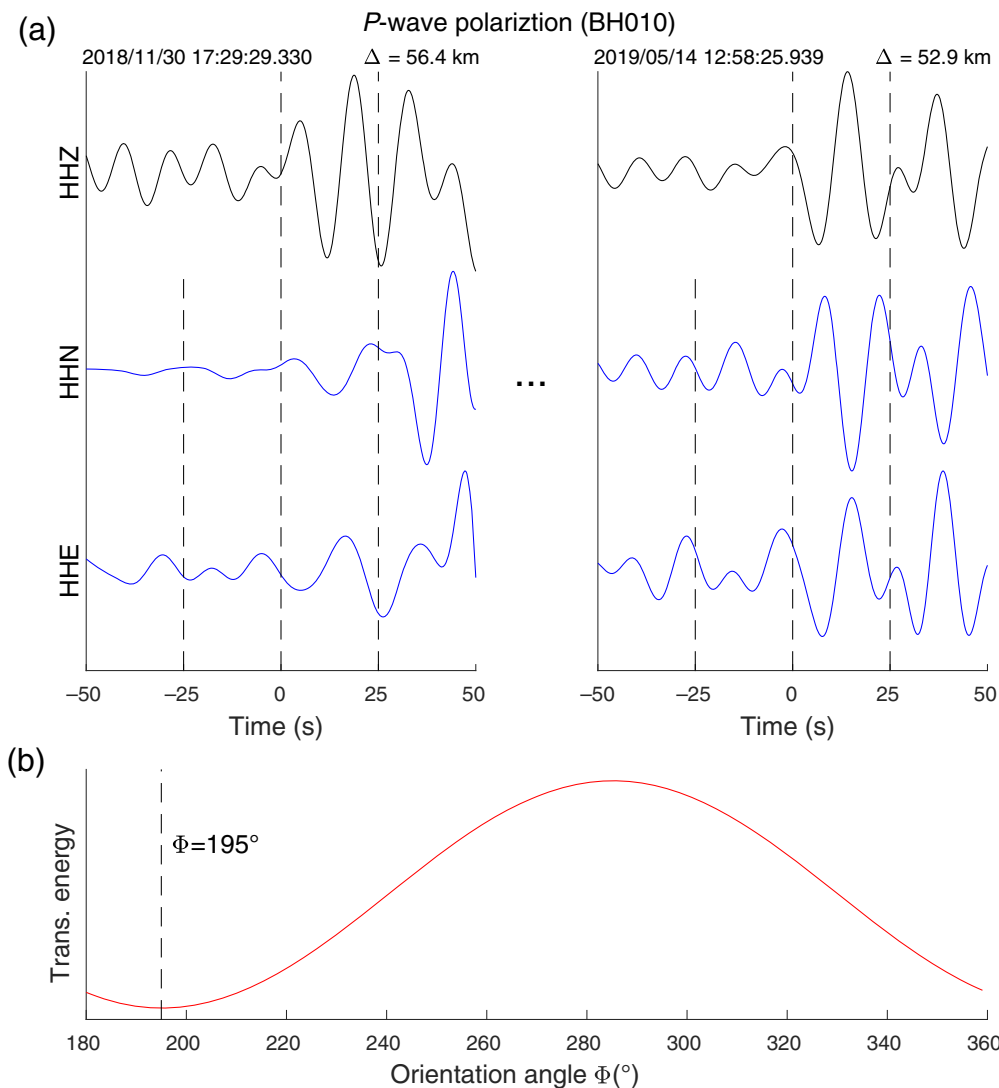


Figure 5. Orientation determination for station BH010 by the particle-motion analysis of initial P -wave arrival. (a) Three-component waveforms from two earthquake events are shown together, with the windows used for signal-to-noise ratio computation and correlation analysis. (b) The summed transverse energy of all the events at the station as a function of orientation angle, and the best angle is obtained by minimizing the summed transverse energy. The color version of this figure is available only in the electronic edition.

in which $S_{jk} = \sum_{\tau=1}^N x_j(\tau)x_k(\tau)$ is the zero-lag cross correlation between two time series x_j and x_k . Usually, it is hard to implement the process by maximizing $C_{z\bar{r}}$ using equation (2), because, the numerator changes in synchronization with $S_{\bar{r}\bar{r}}$ in the denominator, while S_{zz} is constant. It is avoided by introducing a new coefficient that has a well-defined maximum value, as follows:

$$C_{z\bar{r}}^*(\Phi) = \frac{S_{z\bar{r}}}{S_{zz}}. \quad (3)$$

Considering that this value is unbounded, we used equation (2) to assess the quality of the cross correlation, because it has a well-defined range of $[-1, +1]$ (Baker and Stevens, 2004).

For our analyses, altogether, we used 26 earthquake events, including both the earthquakes used in the P -wave analysis with epicentral distance between 5° and 90° and the earthquakes of magnitude ≥ 7.0 between 90° and 175° . We excluded the earthquakes with source depths ≥ 150 km to minimize the risk of overtone contamination and excluded earthquakes with epicentral distances $\leq 5^\circ$ and $\geq 175^\circ$ to avoid bias from near-source or antipodal multipathing effects. We deconvolved all the events with the instrument responses and then passed a band-pass Butterworth filter from 0.02 to 0.04 Hz. Assuming a Rayleigh-wave velocity of 4.0 km/s, we obtained the time windows used for analysis from 20 s before and 600 s after the theoretical arrival time.

Figure 6 shows an example of Rayleigh-wave polarization analysis for station BH010. For each event, we determined the best angle by maximizing the correlation coefficient using equation (3) based on coordinate rotation. After we those results with $C_{z\bar{r}} \geq 0.8$ are left for the statistical analysis. In the remaining dataset, we adopted the median of the angles corresponding to their maximum, as the final result to avoid the bias by outliers. In addition,

we used SMAD, which was defined as the standard deviation of median of the absolute deviations from the data's median for a Gaussian distribution, as the error estimations (Stachnik *et al.*, 2012). Table 1 listed all the results, including the events number used, the best angle, and the SMAD for each station.

AMBIENT-NOISE ANALYSIS

Rayleigh wave can be retrieved from ambient seismic noise records by cross-correlating the cross and diagonal terms of Green's function between station pairs; therefore, the polarization analysis of retrieved Rayleigh wave offers another option to determine the horizontal orientation angle of the seismometer. Zha *et al.* firstly developed this method and applied it at an OBS network in the Eastern Lau Spreading Center (Zha *et al.*, 2013).

TABLE 1

Summary of Sensor-Orientation Angles Estimated from Polarization Analysis

Station	P-Wave			Rayleigh-Wave			Ambient-Noise			Average	
	N	Φ (°)	Error (°)*	N	Φ (°)	Error (°)†	N	Φ (°)	Error (°)‡	Φ (°)	Error (°)§
BH001	12	152.0	8.0	4	147.9	4.8	179	153.0	10.3	151.0	5.1
BH002	8	107.0	7.0	6	105.4	5.4	174	100.0	9.1	104.1	7.0
BH003	4	194.0	6.0	2	186.8	0.0	194	185.9	8.0	188.9	8.1
BH004	16	156.0	8.0	6	148.1	22.1	163	162.6	12.5	155.6	14.5
BH005	10	316.0	10.0	6	309.2	0.0	121	313.2	8.6	312.8	6.8
BH006	15	207.0	9.0	6	219.4	0.0	111	227.6	10.0	218.0	20.6
BH007	3	68.0	4.0	3	54.8	0.0	153	63.2	8.4	62.0	13.2
BH008	15	109.0	9.0	9	85.1	21.4	178	115.5	10.5	103.3	30.4
BH009	3	275.0	8.0	4	240.4	6.4	135	260.5	12.7	258.7	34.6
BH010	15	195.0	9.0	8	193.6	0.0	146	198.5	11.6	195.7	4.9
BH011	5	78.0	10.0	8	43.9	12.5	171	70.7	13.5	64.3	34.1
BH012	11	336.0	8.0	7	334.1	0.0	85	326.4	18.5	332.2	9.6
BH013	14	284.0	11.0	5	267.4	0.0	150	241.3	12.1	264.3	42.7
BH014	17	135.0	11.0	7	116.1	18.4	152	163.9	12.2	138.2	47.8
BH016	17	305.0	8.0	5	302.7	0.0	163	302.1	8.0	303.3	2.9
BH017	10	270.0	10.0	4	267.5	0.0	157	292.4	8.7	276.6	24.9
BH018	13	171.0	7.0	5	171.4	11.2	170	186.8	9.7	176.4	15.8
BH019	14	310.0	8.0	3	318.1	0.0	196	330.7	6.5	319.6	20.7
BH020	15	297.0	7.0	7	287.0	0.0	100	300.1	9.9	294.7	13.1
BH021	12	336.0	9.0	4	314.8	0.0	144	327.4	10.5	326.1	21.2
BH022	12	123.0	12.0	7	110.0	14.3	79	100.6	12.5	111.2	22.4
BH023	13	166.0	9.0	8	172.5	13.5	66	163.6	14.6	167.4	8.9
BH025	10	322.0	15.0	8	316.0	0.0	219	306.5	6.1	314.8	15.5
BH026	18	126.0	7.0	13	127.2	14.5	110	113.4	12.9	122.2	13.8
BH027	11	86.0	7.0	5	83.1	8.2	129	68.2	22.5	79.1	17.8
BH030	4	179.0	5.0	6	176.2	2.9	96	175.5	11.2	176.9	3.5
BH031	15	65.0	10.0	7	66.1	14.5	131	62.5	14.0	64.5	3.6
BH032	13	171.0	8.0	-	-	-	122	172.4	10.1	171.7	1.4

*95% confidence level for 1 degree of freedom per second (Niu and Li, 2011).

†Standard deviation from the median of the absolute deviation (Stachnik et al., 2012).

‡ 2σ confidence level of mean, in degrees equivalent of 95% (Zha et al., 2013).

§Defined as the variation range among the three methods ($\Phi_{\text{Max}} - \Phi_{\text{Min}}$).

Similar to the Rayleigh-wave analysis based on earthquake events, two correlation coefficients are taken as follows:

$$R_{zr}(\Phi) = \frac{\rho(G_{zr}, G_{\bar{z}\bar{z}})}{\sqrt{\rho(G_{zr}, G_{zr})\rho(G_{\bar{z}\bar{z}}, G_{\bar{z}\bar{z}})}}, \quad (4)$$

$$S_{zr}(\Phi) = \frac{\rho(G_{zr}, G_{\bar{z}\bar{z}})}{\rho(G_{\bar{z}\bar{z}}, G_{\bar{z}\bar{z}})}, \quad (5)$$

in which G_{zi} is the stacked cross-correlation function (CCF) between the vertical component of the station serving as source and the i th component of the station serving as receiver, and $\rho(x, y) = \sum_{\tau=1}^N x(\tau)y(\tau)$ is the zero-lag cross correlation between two time series x and y . S_{zr} is used for the estimate of orientation angle, and R_{zr} is used for quality control due to its well-defined range of $[-1, +1]$.

To increase the ray-path coverage in ambient-noise analysis, we combined the data of 325 stations from the ChinArray project nearby Bohai Sea, which are shown as black

square symbols in Figure 1. To avoid the interferences of timing problems by the hardware malfunction in the OBS stations, we used only the ~ 200 days of data before April 2019 for both ChinArray and OBS stations. We calculated the CCFs and stacked them for all station pairs with distances ≥ 60 km. Then, band-pass filtered from 0.05 to 0.1 Hz, the time windows used for correlation analysis were cut, assuming group velocities of 2.5–5 km/s.

Figure 7 illustrates the process of orientation determination using ambient-noise analysis for station BH010. As an example, Figure 7a shows the stacked CCFs of station pair between the station BH010 and a ChinArray station 13910, and, based on these waveform data, Figure 7b shows the variation of two correlation coefficients defined by equations (4) and (5), depending on the changes of orientation angle, and we obtained the best angle at the minimum of S_{zr} . Figure 7c summarizes the results from all station pairs. We used the $R_{zr} > 0.5$ as the quality control criteria and calculated the final estimate of the orientation angle as the circular mean of the refined

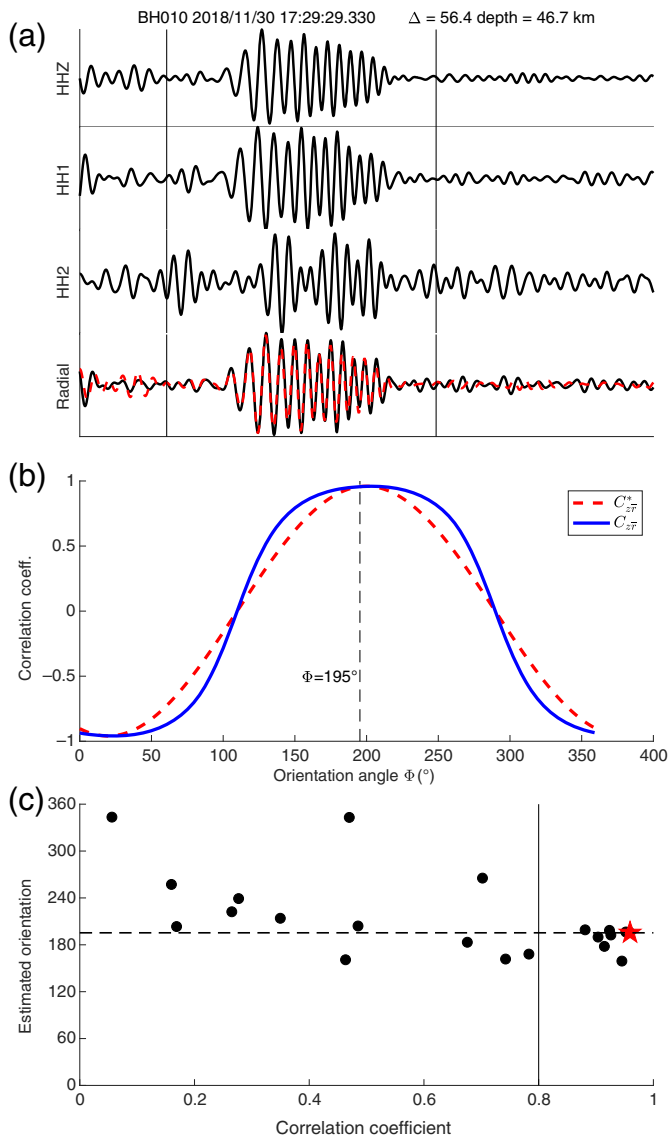


Figure 6. Rayleigh-wave polarization analysis for station BH010. (a) The pre-processed three-component waveforms from a teleseismic event; time windows used were denoted using solid vertical lines; the dashed line of the lowest panel for the radial component showed the Hilbert-transformed vertical component. (b) Correlation coefficient as a function of the orientation angle. The best angle was determined by maximizing the correlation coefficient using earthquake waveforms in (a) based on coordinate rotation. (c) All the obtained estimated orientation angles and the correlation coefficients from all the earthquake events at the station; the dashed horizontal line shows the preferred value for the station based on statistical analysis; the star denotes the result obtained from the event shown in (a,b). The color version of this figure is available only in the electronic edition.

measurements (Berens, 2009). Table 1 listed all the results, including the number of ray paths used, the best angles, and the circular mean errors.

RESULTS AND DISCUSSIONS

Based on the three polarization analysis methods, we obtained effective estimates of the horizontal orientation angle of the

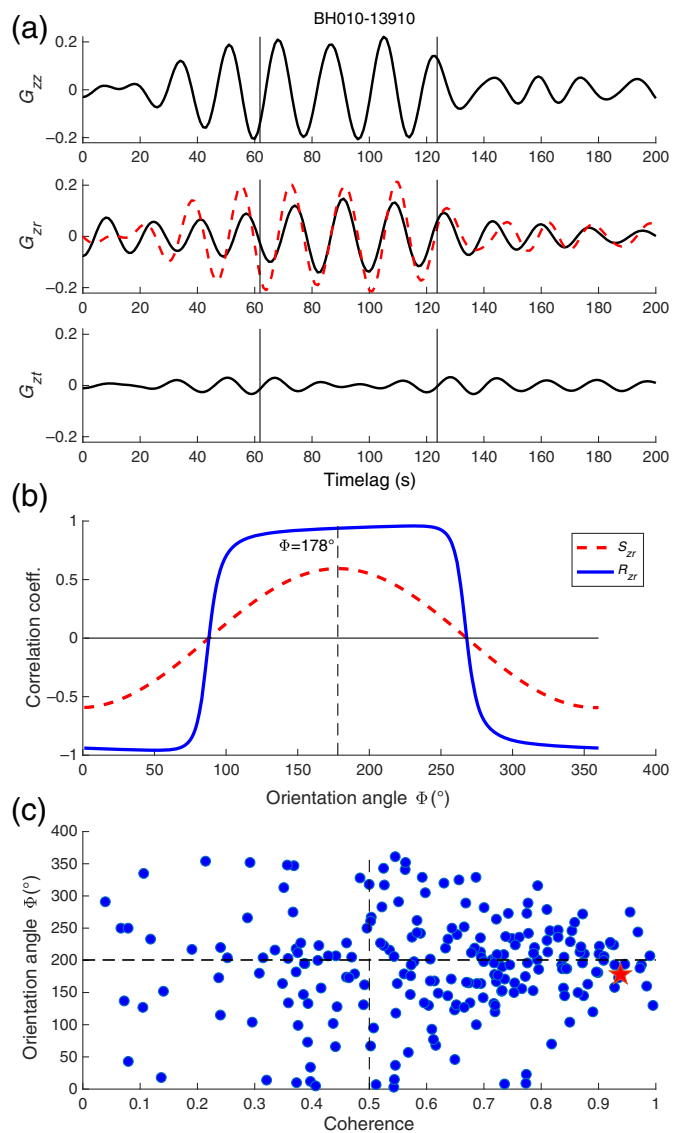


Figure 7. A horizontal orientation determination using ambient-noise analysis for station BH010. (a) The stacked cross-correlation functions in a vertical–radial–transverse coordinate system between station pair BH010 and 13910; The dashed line of middle panel shows 90° phase-shifted G_{zz} ; vertical thin lines indicate the time window used for correlation analysis. (b) Two correlation coefficients in equations (4) and (5) as functions of orientation angle. (c) Orientation measurements of all station pairs for station BH010 as a function of R_{zr} ; the horizontal dashed line marks the circular mean orientation angle as the final result, and the vertical dashed line marks the threshold value for quality control; the result obtained in (a,b) is denoted as a star. The color version of this figure is available only in the electronic edition.

seismometer for 28 out of 29 recovered OBS stations, in which the estimates were not determined for station BH024 owing to instrument failure. We simply average our measurements over three orientation estimates from three analysis methods for a given station, and the variation range among the three methods was given as an error estimate, that is, $\Phi_{\text{Max}} - \Phi_{\text{Min}}$, as shown in the “Average” column of Table 1. Figure 8 illustrates all the obtained orientation angles and their error estimates. Eleven

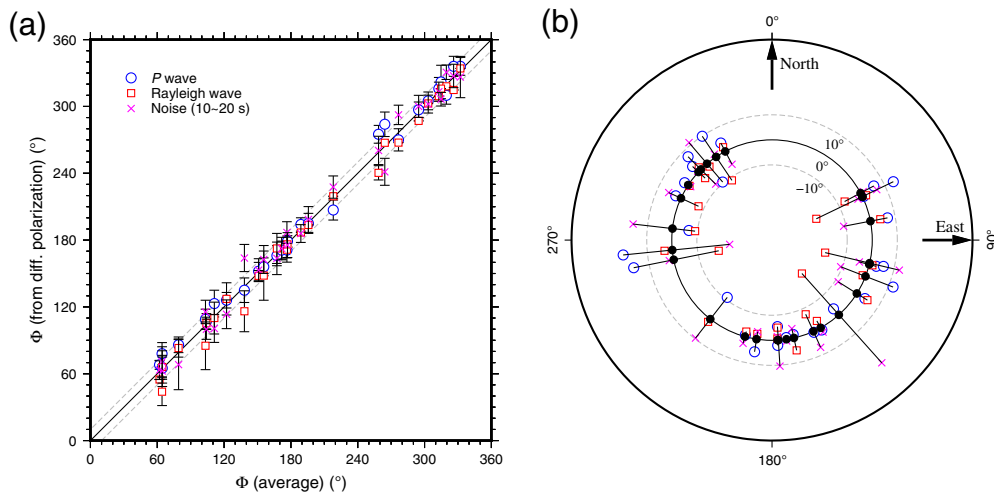


Figure 8. Comparisons of orientation angles from three polarization analyses for all OBS stations. (a) Orientation angles and their error estimates determined from *P*-wave, Rayleigh-wave, and ambient-noise analyses versus average angles, which are the circular mean of those three angles. The solid black line marks $x = y$, and two dashed gray lines mark the $+10^\circ$ and -10° reference. (b) Illustration of (a) in a polar coordinate system with respect to geographic north; the meanings of symbols and colors are the same as in (a). Black solid dots represent the average angle value, as in (a) and Table 1. Gray dashed lines mark the $+10^\circ$ and -10° reference for each measurement. The color version of this figure is available only in the electronic edition.

stations show good agreements from the three methods, and the variations are well below 10° in between. However, there are also some stations, such as BH013 and BH014, showing angle differences up to $\sim 40^\circ$, and the other stations mostly lie between 10° and 25° .

We conceive that the differences of estimations from the three polarization methods mainly come from several causes. First, these methods are based on different seismic observables, and they are subject to various errors and biases. For the *P*-wave polarization, deviations are prone to the appearance of seismic anisotropy and dipping discontinuities within the last wavelength beneath the station (Schulte-Pelkum *et al.*, 2001), especially when the earthquakes used are not azimuth-evenly distributed. We lack the azimuthal coverage of seismic events in quadrants 3 and 4, as shown in Figure 1, and it also hinders us to further investigate these effects. For the Rayleigh-wave polarization, seismic anisotropy, and ray bending effects over the entire path affect the results. For ambient noise, these paths mostly reflect the area between station pairs. In addition, the *P* wave propagates in the 3D earth, and the Rayleigh wave mainly propagates in a 2D surface; they sample different earth structures underground, and these different ray-path propagation effects are unneglectable for the variations of estimation results among the three methods. However, the relatively few numbers of qualified earthquakes and their limited azimuthal coverages hinder us from investigating these effects deeply.

Second, we used different statistical methods during the polarization analyses. For the *P*-wave polarization, we obtained the final estimate by minimizing equation (1), combining all individual events. For the Rayleigh-wave polarization based

on earthquake events and ambient noise, we measured arrival angles for individual earthquakes by minimizing equations (3) and (5) and then obtained the final estimate using circular statistics method. It means that the number of earthquakes or ray paths cannot be a single indication of the validity of each method. For example, the earthquakes used in the *P*-wave analysis seem a bit more than that those in the Rayleigh-wave analysis; however, it does not mean that the *P*-wave results are superior to the Rayleigh-wave results. If we lower the quality control factor for the final statistics during the earthquake-based Rayleigh-wave analysis, the qualified number of earthquake events would significantly rise. If we chose to

adopt the estimation methods based on individual events and data filtering criteria advocated by other researchers (Wang *et al.*, 2016), only less than one-third of stations could obtain effective results for the *P*-wave analysis (see Table S2 and Figure S1). We have been trying to find a balance between the number of qualified measurements and obtaining effective estimations as much as possible for each method. Lastly but not least important, the different noise levels at each station could also be a source of these variations, especially considering that our OBSs were mostly located in the relatively noisier shallow-water area, and this partly explained why we obtained fewer effective estimates from individual events than the other studies (Stachnik *et al.*, 2012).

However, there exists only one true orientation of the seismometer, assuming it does not vary with time, so there should be one angle estimate to be given for later research. During the analysis, we did not find the obvious superiority of one method over the others. The Rayleigh-wave polarization showed a bit higher SNR than others, while having insufficient qualified measurements (mostly less than 10), the ambient noise had the best ray-path coverage, while showing a relatively large scattering of estimation results, and, for the *P* wave, it is not influenced by the timing errors, although the qualified measurements of individual event estimation are not ideal; each method has its merits and demerits. We simply adopted the average value obtained among the three methods and tried to make the final estimate fit with each method in a whole, and the variation among the three methods can thus be seen as an indication of this estimate. In the polarization analysis, there is a trade-off between the accepted final estimates and the number of qualified

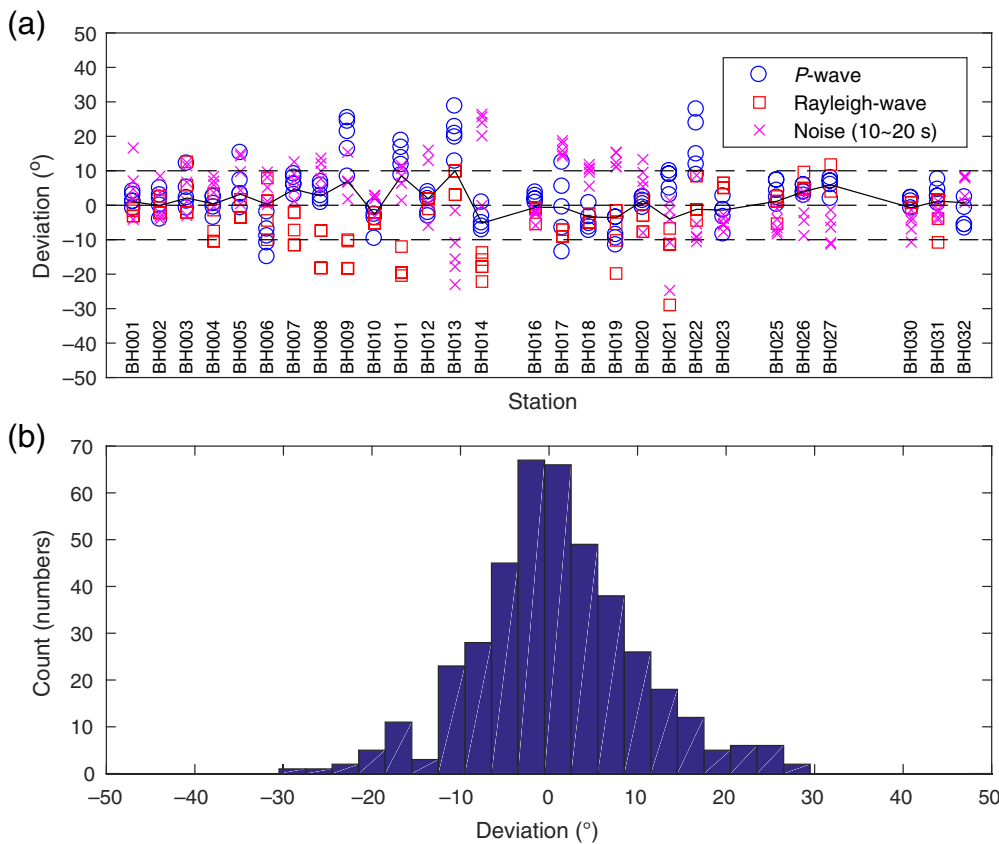


Figure 9. Deviation estimates using different parameters in three polarization analyses methods. (a) Deviations from average orientation angles in Table 1 when using different window lengths, filter bands in the *P*-wave analysis; different cutoff values for quality control in the Rayleigh-wave and ambient-noise analyses during orientation angle determination for each station (see text in the *Results and Discussions* section for details). The thin black line marks the median value of all deviations at a station, and the dashed black lines mark $+10^\circ$ and -10° reference. (b) Distribution of the deviations in (a). The deviations are binned into 3° intervals, and the number in each bin is shown as the height of the bar. The color version of this figure is available only in the electronic edition.

measurements, and some computation parameters influence the results more or less, these include the window length used for analysis, filtering options, quality control factor, and so on; different parameters were used by different researchers (Niu and Li, 2011; Stachnik *et al.*, 2012; Scholz *et al.*, 2017). We conducted a simple test using different parameters to test these susceptibilities, and this could be seen as another indicator of uncertainties for the result obtained at each station. We re-estimated the orientation angles using five different groups of parameters for each method. For the *P*-wave polarization, we varied the window length used for analysis as 15, 25, and 35 s, respectively, when adopting a passband filter 0.04–0.1 Hz, and varied passband filter as 0.03–0.1 Hz and 0.02–0.2 Hz, when adopting window length 25 s as well. For the Rayleigh-wave polarization and ambient-noise analyses, we varied the quality control factor, that is, the correlation coefficient defined by equations (2) and (4) from 0.5 to 0.9, with an interval of 0.1. Figure 9a shows the results for each station, and Figure 9b shows the deviation statistics for all stations with a root mean square deviation of 9.2° . The deviation distribution was consistent with Table 1 and Figure 8, that is,

discern the heterogeneity and anisotropy of earth structures, rather than assuming their distribution to be even or not. Other techniques, such as the use of chip-scale atomic clocks for timing system (Gardner and Collins, 2016) and water-bottom burial installation for lower ambient noise (Araki *et al.*, 2013), should also be valued in OBS-like observations, although they are still costly and time-consuming. If possible, the comprehensive investigations should be coordinated, combining both active and passive seismology, so as to study the underground structures and dynamics more efficiently and robustly.

DATA AND RESOURCES

The earthquake catalogs were accessed through the National Earthquake Information Center (NEIC, <http://earthquake.usgs.gov/earthquakes/search/>, last accessed August 2020). The portable seismic station data were recorded using equipment from China Seismic Array. Seismic data from permanent stations were obtained from the Data Management Centre of China National Seismic Network at the Institute of Geophysics, China Earthquake Administration (<http://www.seisdmc>

those stations with good agreements among the three methods showed a relatively little variation for varying parameters, which proved that angle estimations for these stations are quite robust and reliable.

We obtained orientation angles based on the three polarization methods here, with various uncertainties for each station; this suggests that sensor-orientation determinations from multiple ways in this article are essential and should be dealt with great caution. However, we should be aware that these should and will definitely be solved technically in the future with some new instrumental techniques, such as the introduction of micro-electro-mechanical system gyroscope north finder based on the rotation modulation technique (Spielvogel and Whitcomb, 2015; Zhang *et al.*, 2017). By these techniques, the accuracy of sensor orientation would be hopefully improved one order more than the current determination methods, thus, making it possible to discern

.ac.cn, last accessed August 2020). All the data used in the study are archived in the domain repository at <http://www.seisdmc.ac.cn>. Generic Mapping Tools (GMT) software was used to make some figures (Wessel and Smith, 1998). The supplemental material provides additional tables and figures for *P*-wave polarization analysis, which give greater detail on the earthquakes we used in both *P*-wave and Rayleigh-wave polarization, and the differences and deviation estimates when we adopted different strategies during *P*-wave analysis.

ACKNOWLEDGMENTS

The authors thank captain and crew of the cruises Haohai 0007 and Luqingyujiao 16 involved in the ocean-bottom seismometer (OBS) project in 2018 and 2019. This work was mainly supported by the National Key R&D Program of China (Grant Number 2017YFC1500201) and was partially supported by the Special Fund of the Institute of Geophysics, China Earthquake Administration (Grant Number DQJB19B25), and the National Natural Science Foundation of China (Grant Number 41474047). The authors greatly appreciate the editor-in-chief, Thomas Pratt for his insightful suggestions to the title and key points, and the manuscript coordinator, Betty Schiefelbein for her careful proofreading. The authors also thank two anonymous reviewers for their constructive comments which helped to improve the quality of the manuscript.

REFERENCES

- Anderson, P. N., F. K. Duennebie, and R. K. Cessaro (1987). Ocean borehole horizontal seismic sensor orientation determined from explosive charges, *J. Geophys. Res.* **92**, no. B5, 3573–3579.
- Araki, E., T. Yokobiki, K. Kawaguchi, and Y. Kaneda (2013). Background seismic noise level in DONET seafloor cabled observation network, *Underwater Technology Symposium, IEEE*, ISBN: 978-1-4673-5948-1/13.
- Baker, G. E., and J. L. Stevens (2004). Backazimuth estimation reliability using surface wave polarization, *Geophys. Res. Lett.* **31**, L09611, doi: [10.1029/2004GL019510](https://doi.org/10.1029/2004GL019510).
- Berens, P. (2009). CircStat: A MATLAB toolbox for circular statistics, *J. Stat. Software* **31**, no. 10, 1–21.
- Chen, L., T. Wang, L. Zhao, and T. Zheng (2008). Distinct lateral variation of lithospheric thickness in the northeastern North China Craton, *Earth Planet. Sci. Lett.* **267**, 56–68.
- Deng, Q., P. Zhang, Y. Ran, X. Yang, W. Min, and L. Chen (2003). Active tectonics and earthquake activities in China, *Earth Sci. Front.* **10**, no. S1, 66–73.
- Eckström, G., and R. W. Busby (2008). Measurements of seismometer orientation at USArray transportable array and backbone stations, *Seismol. Res. Lett.* **79**, 554–561.
- Fontaine, F. R., G. Barruol, B. L. N. Kennett, G. H. R. Bokelmann, and D. Reymond (2009). Upper mantle anisotropy beneath Australia and Tahiti from *P* wave polarization: Implications for real-time earthquake location, *J. Geophys. Res.* **114**, no. B3, doi: [10.1029/2008JB005709](https://doi.org/10.1029/2008JB005709).
- Gardner, A. T., and J. A. Collins (2016). A second look at Chip Scale Atomic Clocks for long term precision timing, *Proc. of OCEANS 2016 MTS/IEEE Monterey*, Monterey, California, 1–9.
- Hou, G., and K. R. Hari (2014). Mesozoic-Cenozoic extension of the Bohai Sea: Contribution to the destruction of North China craton, *Front. Earth Sci.* **8**, no. 2, 202–215.
- Jurkevics, A. (1988). Polarization analysis of three-component array data, *Bull. Seismol. Soc. Am.* **78**, 1725–1743.
- Kennett, B. L. N. (Compiler and Editor) (1991). *IASPEI 1991 Seismological Tables*, Bibliotech, Canberra, Australia, 167, doi: [10.1111/j.1365-3121.1991.tb00863.x](https://doi.org/10.1111/j.1365-3121.1991.tb00863.x).
- Laske, G. (1995). Global observation of off-great-circle propagation of long period surface waves, *Geophys. J. Int.* **123**, 245–259.
- Liu, L., T. Hao, C. Lü, Q. You, J. Pan, F. Wang, Y. Xu, C. Zhao, and J. Zhang (2015). Crustal structure of Bohai Sea and adjacent area (North China) from two onshore-offshore wide-angle seismic survey lines, *J. Asian Earth Sci.* **98**, 457–469.
- Niu, F., and J. Li (2011). Component azimuths of the CEArray stations estimated from *P*-wave particle motion, *Earthq. Sci.* **24**, 3–13, doi: [10.1007/s11589-011-0764-8](https://doi.org/10.1007/s11589-011-0764-8).
- Scholz, J.-R., G. Barruol, F. R. Fontaine, K. Sigloch, and W. Crawford (2017). Orienting ocean-bottom seismometers from *P*-wave and Rayleigh wave polarizations, *Geophys. J. Int.* **208**, 1277–1289.
- Schulte-Pelkum, V., G. Masters, and P. Shearer (2001). Upper mantle anisotropy from long-period *P* polarization, *J. Geophys. Res.* **106**, no. B10, 21,917–21,934, doi: [10.1029/2001JB000346](https://doi.org/10.1029/2001JB000346).
- Spielvogel, A. R., and L. L. Whitcomb (2015). Preliminary results with a low-cost fiber-optic gyrocompass system, *Oceans, IEEE*, ISBN: 978-0-9339-5743-5.
- Stachnik, J. C., A. F. Sheehan, D. W. Zietlow, Z. Yang, J. Collins, and A. Ferris (2012). Determination of New Zealand ocean bottom seismometer orientation via Rayleigh-wave polarization, *Seismol. Res. Lett.* **83**, 704–713, doi: [10.1785/0220110128](https://doi.org/10.1785/0220110128).
- Sumy, D., J. Lodewyk, R. Woodward, and B. Evers (2015). Ocean-bottom seismograph performance during the Cascadia initiative, *Seismol. Res. Lett.* **86**, no. 5, 1238–1246.
- Wang, X., Q. Chen, J. Li, and S. Wei (2016). Seismic sensor misorientation measurement using *P*-wave particle motion: An application to the NECsaids array, *Seismol. Res. Lett.* **87**, no. 4, 901–911.
- Webb, S. C., and W. C. Crawford (2010). Shallow-water broadband OBS seismology, *Bull. Seismol. Soc. Am.* **100**, no. 4, 1770–1778.
- Wessel, P., and W. H. F. Smith (1998). New, improved version of generic mapping tools released, *Eos Trans. AGU* **79**, no. 47, 579.
- Wu, F., J. Yang, Y. Xu, S. A. Wilde, and R. J. Walker (2019). Destruction of the North China Craton in the Mesozoic, *Ann. Rev. Earth Planet. Sci.* **47**, no. 1, 173–195.
- Zha, Y., S. C. Webb, and W. Menke (2013). Determining the orientations of ocean bottom seismometers using ambient noise correlation, *Geophys. Res. Lett.* **40**, 3585–3590, doi: [10.1002/GRL.50698](https://doi.org/10.1002/GRL.50698).
- Zhang, Y., B. Zhou, M. Song, B. Hou, H. Xing, and R. Zhang (2017). A novel MEMS gyro north finder design based on the rotation modulation technique, *Sensors* **17**, no. 5, 973, doi: [10.3390/s17050973](https://doi.org/10.3390/s17050973).
- Zhu, G., H. Yang, J. Lin, and Q. You (2020). Determining the orientation of ocean-bottom seismometers on the seafloor and correcting for polarity flipping via polarization analysis and waveform modeling, *Seismol. Res. Lett.* **91**, no. 2A, 814–825.
- Zhu, R., Y. Xu, G. Zhu, H. Zhang, Q. Xia, and T. Zheng (2012). Destruction of the North China Craton, *Sci. China Earth Sci.* **55**, 1565–1587.

Manuscript received 6 May 2020
Published online 22 September 2020